


RESEARCH ARTICLE

Fluorine MR Imaging Probes Dynamic Migratory Profiles of Perfluorocarbon-Loaded Dendritic Cells After Streptozotocin-Induced Inflammation

Shweta Saini¹, An-Sofie Vanherwegen², Sayuan Liang^{1,3}, Rein Verbeke⁴, Hannelie Korf⁵, Ine Lentacker⁴, Stefaan C. De Smedt⁴, Conny Gysemans², and Uwe Himmelreich¹ 

¹Biomedical MRI/Molecular Small Animal Imaging Center (MoSAIC), KU Leuven, Leuven, Belgium

²Clinical and Experimental Endocrinology, CHROMETA, KU Leuven, Leuven, Belgium

³Philips Research China, Shanghai, China

⁴General Biochemistry and Physical Pharmacy, University of Ghent, Ghent, Belgium

⁵Laboratory of Hepatology, CHROMETA, KU Leuven, Leuven, Belgium 2022

Abstract

Purpose: The pathogenesis of type 1 diabetes (T1D) involves presentation of islet-specific self-antigens by dendritic cells (DCs) to autoreactive T cells, resulting in the destruction of insulin-producing pancreatic beta cells. We aimed to study the dynamic homing of diabetes-prone DCs to the pancreas and nearby organs with and without induction of pancreatic stress in a T1D susceptible model of repeated streptozotocin (STZ) injection. **Procedures:** In vitro labeling of activated bone marrow-derived DCs (BMDCs) from NOD (Nonobese diabetes) mice was performed using zonyl perfluoro-15-crown-5-ether nanoparticles (ZPFCE-NPs). Internalization of particles was confirmed by confocal microscopy. Two groups of NOD.SCID (nonobese diabetic/severe combined immunodeficiency) mice with (induced by low dose STZ administration) or without pancreatic stress were compared. Diabetogenic BMDCs loaded with BDC2.5 mimotope were pre-labeled with ZPFCE-NPs and adoptively transferred into mice. Longitudinal in vivo fluorine MRI (¹⁹F MRI) was performed 24 h, 36 h and 48 h after transfer of BMDCs. For ex vivo quantification of labeled cells, ¹⁹F NMR and flow cytometry were performed on dissected tissues to validate in vivo ¹⁹F MRI data. **Results:** In vitro flow cytometry and confocal microscopy confirmed high uptake of nanoparticles in BMDCs during the process of maturation. Migration/homing of activated and ZPFCE-NP- labeled BMDCs to different organs was monitored and quantified longitudinally, showing highest cell density in pancreas at 48-h time-point. Based on ¹⁹F MRI, STZ induced mild inflammation in the pancreatic region, as indicated by high accumulation of ZPFCE-NP-labeled BMDCs in the pancreas when compared to the vehicle group. Pancreatic draining lymph nodes showed elevated homing of labeled BMDCs in the vehicle groups in contrast to the STZ group after 72 h. The effect of STZ was confirmed by increased blood glucose levels. **Conclusion:** We showed the potential of ¹⁹F MRI for the non-invasive visualization and quantification of migrating immune cells in models for pancreatic inflammation after STZ administration. Without any intrinsic background signal, ¹⁹F MRI serves as a highly specific imaging tool to study the migration of diabetic-prone BMDCs in T1D models in vivo. This approach could particularly be of interest for the longitudinal assessment of established or novel anti-inflammatory therapeutic approaches in preclinical models.

Key words Type 1 diabetes · Dendritic cells · ¹⁹F MRI · Pancreas · Cell imaging

Introduction

Type 1 diabetes (T1D) is an autoimmune disease caused by the T cell-mediated destruction of insulin-producing pancreatic beta cells. The disease usually starts at a young age and during adolescence [1–3]. The exact pathogenesis of T1D is still not fully understood, but it is believed to be a complex interplay between genetic risk factors and environmental triggers [4–6]. The initiation of the disease involves the recruitment of immune cells surrounding and invading the islets of Langerhans [7, 8]. Insulinitis can also be induced by chemicals, such as streptozotocin (STZ) leading to acute or chronic injury of pancreatic tissue [9, 10].

In this study, we have applied this widely used model of repeated low-dose injection of STZ. In this model, mice gradually develop hyperglycemia, which is associated with inflammatory changes of pancreatic islets involving macrophages and T cells. Broad infiltration of macrophages has been shown to induce a pro-inflammatory state in STZ-induced hyperglycemic mice [11]. Moreover, chemokines are expressed in the islets of mice treated with multiple low doses of STZ before the development of diabetes. It has been proposed that initial burst in the expression of chemokines contributes to the further recruitment of inflammatory cells and the destruction of the islets [12]. Proportions of dendritic cells and B cells are increased from day three after STZ injection. Later, the proportions of T cells are increased from day seven after STZ injection, suggesting that the innate immune cells precede adaptive immune cell response in this model [13]. Here, we investigated the trafficking of syngeneic autoantigen (BDC2.5)-loaded dendritic cells to the pancreas of NOD.SCID mice. Dendritic cells (DCs) are professional antigen-presenting cells that possess the ability to link innate and adaptive immunity by priming antigen-specific T cell responses. In addition, DCs are also involved in the induction of both central and peripheral tolerance [14–17]. Studies in mouse models of T1D show that DCs are the main culprits for triggering pancreatic inflammation as they present islet-specific-autoantigens to islet antigen-specific T cells in the draining pancreatic lymph nodes (pLN) [18, 19]. The pathogenesis of T1D is well studied in murine models of the disease [20]. Many preclinical and clinical studies have investigated the multifactorial function of DCs during onset and progression of this autoimmune disease. While *in vivo* imaging has been employed for tracking DC migration in preclinical models and in the clinic [21–23], the kinetics of diabetogenic DCs homing to the pancreas and pLN are still not fully understood also due to only a limited number of studies applying these imaging methods to the longitudinal *in vivo* tracking of cells in diabetes models [24].

In this regard, non-invasive imaging of immune cells provides a powerful tool to elucidate the inflammatory processes taking place in the pancreatic region upon an inflammatory trigger [25–28]. Over the past decade, imaging of the pancreas in rodent models has improved by the use of magnetic

resonance imaging (MRI), positron emission tomography (PET) or optical imaging techniques mainly based on novel contrast agents and tracers [26, 29–31]. Although, proton (^1H) MRI is often employed for the visualization of inflammation in brain [32, 33], its application in the abdomen remains elusive due to potentially misleading hypointense background signal. In contrast, it has been shown that fluorine-19 MR imaging (^{19}F MRI) can track *in vivo* inflammatory events occurring in various diseases with the help of *in vitro* and *in vivo* cell labeling applications using fluorine-based contrast agents [34–38]. In this regard, ^{19}F MRI proves to be an effective and specific method to detect immune cells and their homing even in the abdomen by applying sensitive fluorine contrast agents like perfluorocarbons (PFCs). Perfluoro-15-crown-5-ether-based nanoparticles (PFCE-NPs) contain 20 identical fluorine atoms and exhibit inert chemical properties, permitting its wide use for the labeling and tracking of immune cells [39, 40]. The development of dedicated clinical ^{19}F MR coils facilitates the dynamic tracking of PFC-loaded DCs in tumor patients undergoing immunotherapy [41, 42]. Therefore, it is imperative to combine ^{19}F MRI with biologically compatible fluorine contrast agents generating a relatively high signal-to-noise ratio for the evaluation of underlying inflammatory reactions in murine models of T1D. In the current manuscript, we employed newly synthesized PFCE-NPs based on zonyl fluorosurfactant to generate zonyl perfluoro-15-crown-5-ether nanoparticles (ZPFCE-NPs). Compared to other PFCE-NPs, ZPFCE-NPs showed better uptake properties and excellent biocompatibility [43]. ZPFCE-NPs were used to visualize and quantify the homing of activated, labeled murine bone marrow-derived DCs (BMDCs) *in vivo* in a non-invasive manner in immunodeficient diabetes-prone mice using ^{19}F MRI.

Materials and Methods

Synthesis and Characterization of Fluorinated Zonyl-PFCE Nanoparticles

The synthesis of biochemically inert perfluoro-15-crown-5-ether nanoparticles (PFCE-NPs) was performed as described previously [44]. The anionic ZPFCE-NPs were prepared by incorporating additional zonyl FSP® surfactant to the PFCE particles [43]. For the *in vitro* and *in vivo* experiments, ZPFCE-NPs were coupled with a DiR fluorescent dye (Molecular Probes, Invitrogen, Merelbeke, Belgium). The ZPFCE-NPs were subjected to a size and zeta potential quality control using a Malvern Zetasizer nano-ZS (Malvern Instruments Ltd, Worcestershire, UK).

Animals

Non-obese diabetic (NOD) mice ($n = 30$) were originally obtained from Prof. Wu (Department of Endocrinology,

Peking Union Medical College Hospital, Beijing, China) and were bred and housed under semi-barrier conditions in the animal facility of KU Leuven. NOD.CB17-Prkdcscid/J (NOD.SCID) mice ($n = 18$) were bred under specific pathogen-free conditions from stocks purchased from The Jackson Laboratory (Bar Harbor, ME, USA) in the animal facility of KU Leuven. Animals were housed at 22 °C on a fixed 12 h light–dark cycle, with ad libitum access to food and water. Experiments were performed in accordance with regional, national and international standards on animal welfare, in particular, European Union Directive 2010/63/EU. Experiments were approved and overseen by the Animal Care and Ethical Committees of the KU Leuven. To assess isograft function, blood glucose values were measured every other day with a precision blood glucose meter (Glucocard memory 2, Menarini, Florence, Italy).

Generation and Labeling of BMDCs with ZPFCE-NPs

Bone marrow-derived dendritic cells (BMDCs) were generated from 3 to 4-week-old NOD mice as previously described [45]. In brief, bone marrow precursor cells were isolated from the femora and tibiae and subsequently cultured in RPMI 1640 medium supplemented with Glutamax-I, 25 mM HEPES (Thermo Fisher Scientific, Merelbeke, Belgium), 10% heat-inactivated fetal calf serum (FCS, Merck, Darmstadt, Germany), 100 U/ml Penicillin, 100 mg/ml

Streptomycin (Thermo Fisher Scientific, Merelbeke, Belgium) and 50 μM 2-mercaptoethanol (Thermo Fisher Scientific, Merelbeke, Belgium) in the presence of 20 ng/ml murine recombinant (r) IL-4 (Peprotech, Rocky Hill, NJ, USA) and 20 ng/ml murine rGM-CSF (Peprotech, Rocky Hill, NJ, USA) for 8 days. At day 3 and day 6, cytokines were refreshed. At day 8 of BMDC culture, CD11c+ cells were isolated by positive magnetic cell sorting (MACS, Miltenyi, Biotec, St. Louis, MO, USA). Subsequently, cells were matured for 24 h in the presence of 1 μg/ml lipopolysaccharide (LPS, Merck, Darmstadt, Germany) and 20 ng/ml murine interferon r(IFN)-γ (both from Peprotech, Rocky Hill, NJ, USA) (Fig. 1).

During maturation, BMDCs were labeled with 20 mM of ZPFCE-NPs for 24 h. On day 9, mature BMDCs were harvested and pulsed with 10 μg/ml of BDC2.5 mimotope (AnaSpec, Fremont, CA, USA) for 2 h at 37 °C prior to in vivo injection.

Flow Cytometry

The in vitro labeling of BMDCs with ZPFCE-NPs was optimized at various concentrations (0, 1, 5 and 20 mM) and validated by flow cytometry. For the identification of ZPFCE-NP-labeled DCs, 2.5×10^5 BMDCs were first incubated with Fc receptor blocking antibody (Thermo Fisher Scientific, RRID:AB_467134) to minimize non-specific binding. In order to distinguish DCs from other immune cells

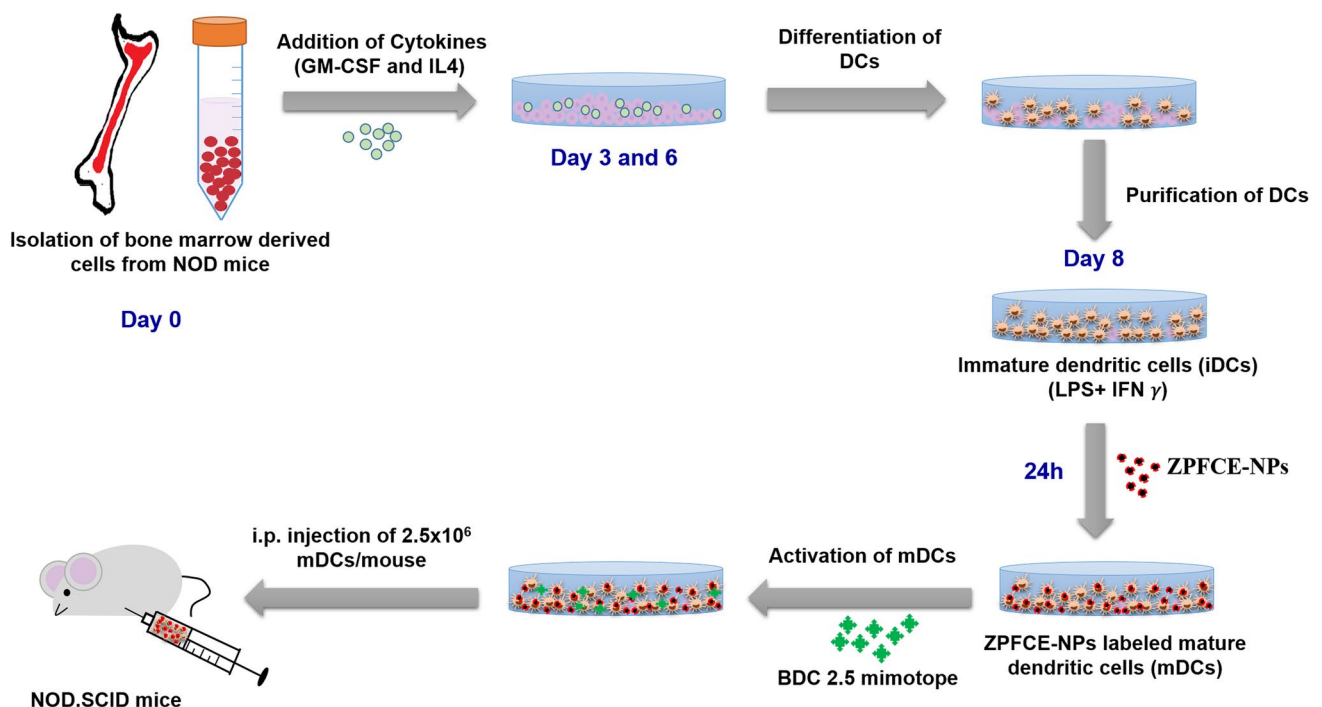


Fig. 1 Schematic representation showing harvesting of bone marrow derived and ZPFCE-NP-labeled dendritic cells. Antigen loaded pre-labeled dendritic cells were adoptively transferred into the NOD.SCID murine model for follow-up by ¹⁹F MRI. IL interleukin, mDCs mature dendritic cells, BMDCs bone marrow derived dendritic cells, ZPFCE-NPs zonyl perfluoro-15-crown-5-ether nanoparticles

and to evaluate the purity of the DC population, cells were surface stained with a cocktail of the following antibodies against major histocompatibility complex (MHC-II) I-A/I-E (Thermo Fisher Scientific, RRID:AB_465231) and CD11c (Thermo Fisher Scientific, RRID:AB_465553). Doublets were excluded based on signal height and width. Dead cells were stained by Zombie Yellow Fixable Viability Kit (BioLegend, 423,104, San Diego, CA, USA) according to the manufacturer's guidelines. They were excluded from analysis. Samples were read on a Gallios™ Flow Cytometer (Beckman Coulter, Analis, Suarlée, Belgium) and analyzed with the FlowJo software v10.1 (TreeStar, Ashland, OR, USA).

Confocal Microscopy

BMDCs labeled with ZPFCE-NPs were fixed in 4% PFA. Microscopy was performed using a confocal microscope (Nikon Eclipse A1R microscope, VIB 11, Center for the Biology of Disease, KU Leuven). Data were analyzed using the NIS Element software v4.10 (Nikon, Tokyo, Japan) and processed in Fiji software v1.49a (SC, USA).

MR Imaging of Phantoms and Longitudinal In Vivo Follow-Up of ZPFCE-NPs-Labeled BMDCs Using ¹⁹F MRI

Phantoms were prepared by embedding ZPFCE-NP-labeled BMDCs using agarose (2%) gel in Eppendorf tubes at 1×10^6 , 2.5×10^6 and 5×10^6 cells ml⁻¹ concentrations as described [46]. An Eppendorf tube filled with agar was used as a positive control. For in vivo ¹⁹F MR imaging, one group of 5 to 6-week-old NOD.SCID female mice ($n = 5$) was injected intraperitoneally (i.p.) with 50 mg/kg streptozotocin (STZ) in citrate buffer, 3 days prior the adoptive transfer of DCs. The vehicle group (control group with no pancreatic inflammation) of 5 to 6-week-old NOD.SCID female mice ($n = 5$) received i.p. injections of sterile saline. To study pancreatic stress in this model, blood glucose values were measured every other day with a precision blood glucose meter (Glucocard memory 2, Menarini, Florence, Italy) in a separate group of animals ($n = 4$ for each STZ injected and vehicle group). After 72 h, mice were engrafted i.p. with 2.5×10^6 BDC2.5-mimotope-loaded BMDCs derived from NOD mice and labeled with ZPFCE-NPs (Fig. 2). Control mice ($n = 3$) were injected i.p. with sterile saline. For in vivo ¹⁹F MR imaging, animals were anesthetized by i.p. administration of a solution of 45–60 mg kg⁻¹ ketamine (Nimatek, Eurovet Animal Health, AE Bladel, The Netherlands) and 0.6–0.8 mg kg⁻¹ medetomidine (Domitor, The Orion Pharma, Espoo, Finland). In vivo MR images were acquired at 24 h, 36 h and 48 h from control mice and mice engrafted with ZPFCE-NP-labeled BMDCs using a purpose-built dual tuned ¹H/¹⁹F MR surface coil to acquire anatomical and fluorine images of the abdominal region [47].

All MR experiments were performed on a 9.4 T preclinical MR scanner (Bruker Biospec 94/20, Ettlingen, Germany). For radiofrequency transmission and reception, a home built, inductively coupled, saddle shaped surface coil, tunable from 376 MHz for ¹⁹F to 400 MHz for ¹H was used for all experiments (see also Suppl. Figure 1) using a 2D RARE (Rapid Acquisition with Relaxation Enhancement) sequence with the following acquisition parameters: coronal slice orientation; for ¹H MRI: repetition time (TR) = 3500 ms, echo time (TE) = 6.121 ms, RARE factor = 8, in plane spatial resolution = 0.195 mm × 0.156 mm, slice thickness = 1 mm and for ¹⁹F MRI: TE = 4.86 ms, RARE factor = 16, TR = 5388 ms, spatial resolution = 1.56 mm × 1.25 mm, slice thickness = 2 mm. Respiration rate and rectal body temperature of all animals were monitored throughout the experiment and maintained at 60–90 min⁻¹ and at 37 °C, respectively.

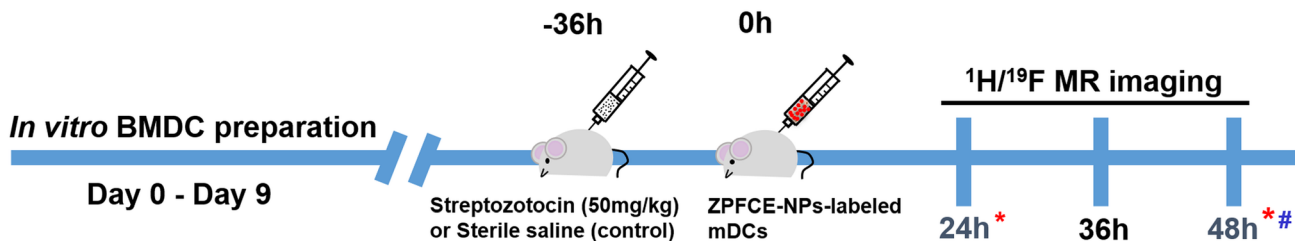
A reference Eppendorf tube (Eppendorf, Rotselaar, Belgium) containing 20 mM ZPFCE-NPs embedded in 1% agar (Merck, Darmstadt, Germany) was placed parallel to the lower abdomen and was used for the quantification of fluorine concentrations. After the MR data acquisition, anesthesia was reversed by i.p. injections of atipamezole (Antisedan, The Orion Pharma, Espoo, Finland).

Quantification of In Vivo ¹⁹F MR Images

¹H MR images were co-registered to ¹⁹F MR images using MeVislab software v2.6.1 (MeVis Medical Solutions AG, Bremen, Germany). An interval threshold value (three times higher than the background noise) was applied to all ¹⁹F MR images. ¹⁹F MR images were masked using a Gaussian filter. The regions of interest containing fluorine signal were delineated, and the mean of signal intensities were quantified using Fiji software, v1.49a (SC, USA). Fluorine signal was quantified as the number of fluorine atoms/pixel in the organs with high ZPFCE-NP accumulation (pancreatic region and liver) based on the overlay of ¹⁹F and anatomical ¹H MR images relative to the external reference of known concentration. For the identification of the pancreas and pLN, surrounding organs were identified and delineated in the ¹H MR images. Regions were then transferred to the co-registered ¹⁹F MR images for the quantification. The slice orientation and field-of-view were kept the same for exact overlay of MR images.

Ex Vivo Quantification of ZPFCE-NP-Labeled BMDCs in Excised Organs Using Flow Cytometry

A separate cohort of animals was used for ex vivo quantification of ZPFC-NP-labeled BMDCs by flow cytometry in parallel to the mice imaged using ¹⁹F MRI. Pancreas and pLN were extracted from mice (control animals ($n = 3$), vehicle- and STZ-treated NOD.SCID mice ($n = 5$ each)) 24 h and 48 h after injection of BDC2.5 mimotope-loaded ZPFCE-NPs-labeled BMDCs. Pancreases were minced into small fragments and digested in pre-warmed digestion



* *Ex vivo* Flow Cytometry

Ex vivo ^{19}F NMR

Fig. 2 Experimental timeline showing the induction of pancreatic stress by streptozotocin (STZ) and administration of ZPFCE-NP-labeled BMDCs for their longitudinal follow-up. ZPFCE-NP-labeled BMDCs were quantified *ex vivo* by flow cytometry at 24 h and 48 h and *in vivo* using ^{19}F MR imaging at 24 h, 36 h and 48 h. *Ex vivo* ^{19}F NMR spectroscopy of liver samples was performed at 48 h after euthanizing the animals

medium containing 1 mg/ml collagenase VIII (SERVA, Heidelberg, Germany) and $20 \mu\text{g ml}^{-1}$ DNase I (AppliChem, Darmstadt, Germany). Enzymatic digestion was performed for 30 min at 37°C under continuous rotation using a rotarod. All single-cell suspensions were passed through a $70\text{-}\mu\text{m}$ strainer (Miltenyi Biotec, Leiden, The Netherlands). Red blood cells were lysed using NH_4Cl at 37°C . For flow cytometry analysis, cells were stained as described above.

Ex Vivo ^{19}F NMR Spectroscopy

ZPFCE-NPs-labeled BMDCs that migrated to the liver 48 h post injection were quantified from excised tissue samples by determining fluorine concentrations using *ex vivo* ^{19}F NMR spectroscopy. Livers were dissected and homogenized in PBS solution and transferred to 5-mm NMR tubes (Wilmad, Vineland, NJ, USA). For the acquisition of data, an NMR spectrometer (400 MHz) with an Avance II console (Bruker Biospin GmbH, Rheinstetten, Germany) was used, operating at a frequency of 376.50 MHz for ^{19}F NMR. The following parameters were used for data acquisition: relaxation delay: 5 s, number of acquisitions: 1024, spectral width: 350 ppm and 128 k data points. A reference Eppendorf containing 20 mM ZPFCE-NPs was added for the quantification. Data analyses were performed after phase and baseline correction by peak integration using the TopSpin software (Bruker Biospin, Rheinstetten, Germany).

Statistical Analysis

Statistical significance was determined using one-way analysis of variance (ANOVA) tests with Bonferroni's multiple comparison tests. Results were expressed as mean values \pm SEM. All statistical analyses were performed using GraphPad Prism v5.3 (GraphPad software, La Jolla, CA, USA).

Results

Composition and Quantification of Fluorinated ZPFCE Nanoparticles for BMDCs Labeling

Anionic ZPFCE-NPs were synthesized by addition of the zonyl FSP fluorosurfactant to the lipid layers of PFCE-NPs in order to reduce their diameter to ~ 280 nm. The zeta potential of ZPFCE-NPs was -75 mV, indicating a high stability of these particles (Fig. 3a). The size distribution of ZPFCE-NPs is indicated by the polydispersity index (PdI) of ~ 0.312 .

The near infrared DiR fluorescent dye was incorporated in the particles in order to confirm the labeling of BMDCs. For the quantification of fluorine atoms taken up by BMDCs, *in vitro* ^{19}F MRI phantom experiments were performed. BMDCs were labeled with 20 mM ZPFCE-NPs for 24 h, and cells were embedded in agar at quantities of 1×10^6 cell ml^{-1} , 2.5×10^6 cell ml^{-1} and 5×10^6 cell ml^{-1} , respectively for ^1H and ^{19}F MR imaging. (Fig. 3b–c). Here, we show the ^{19}F MR signal with a linear correlation to the number of labeled cells embedded in the agar at all cell concentrations. No further increase in the number of fluorine atoms was observed for cell concentrations as high as 5×10^6 cells ml^{-1} .

In Vitro Characterization of ZPFCE-NPs Labeled BMDCs

In vitro labeling experiments were performed to find the optimal procedure to achieve high cellular uptake. After purification of CD11c^+ cells on day 8, BMDCs were either matured for 24 h in the presence of ZPFCE-NPs (indicated as iDCs) or matured for 24 h after which ZPFCE-NPs were added for an additional 24 h (indicated as mDCs). For both conditions, 1 mM, 5 mM and 20 mM ZPFCE-NPs were used. This concentration range was based on previous experiments that showed excellent cell labeling and biocompatibility [43]. Comparison of viable cells with and without ZPFCE-NP

Formulation and characterization of ZPFCE-NPs

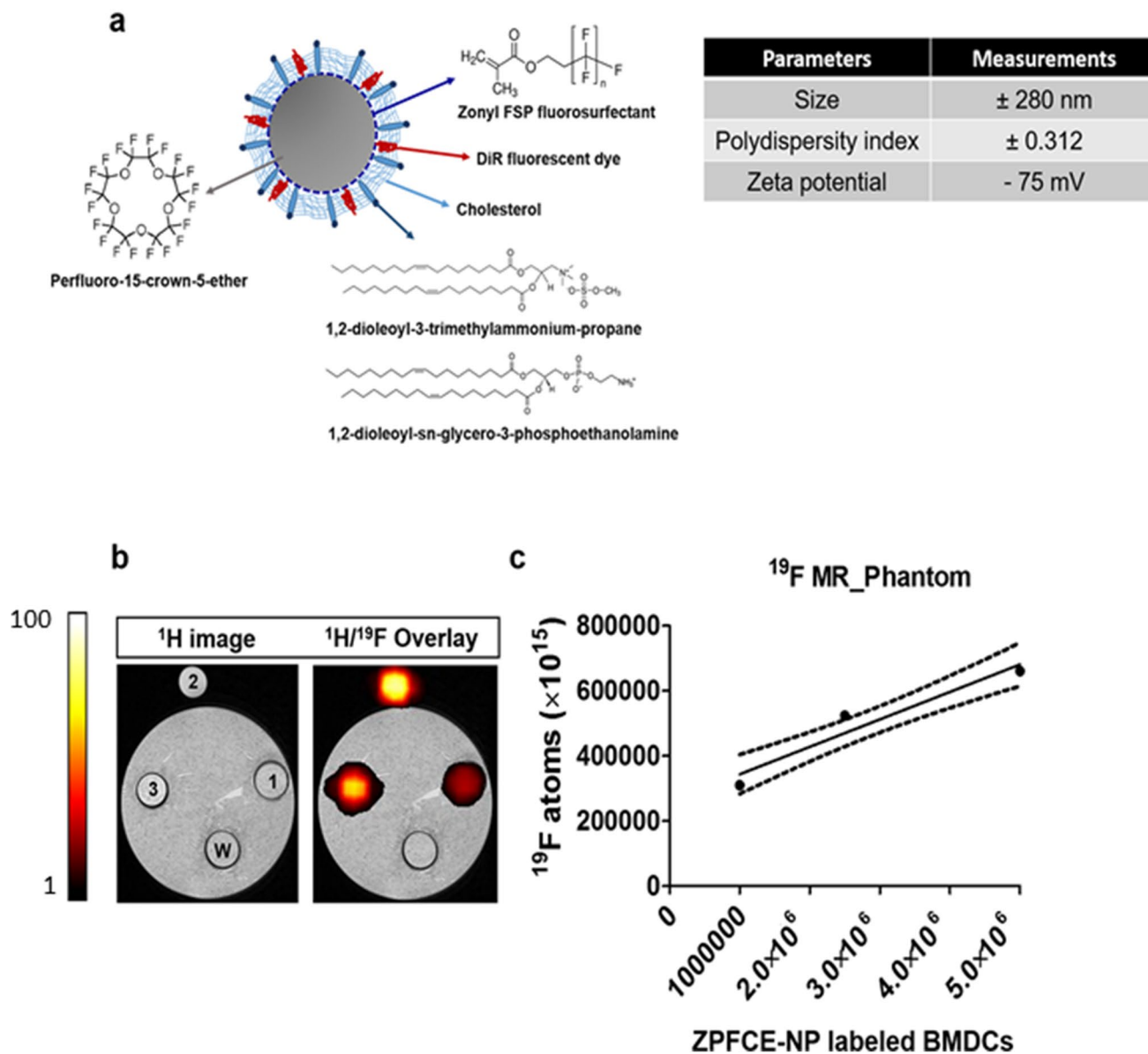


Fig. 3 Chemical composition, characteristic features of ZPFCE-NPs and in vitro characterization by ^{19}F MR imaging of ZPFCE-NP-loaded BMDCs in agar phantoms. **a** Illustrative image of lipid encapsulated PFCE-NPs consisting of perfluoro-15-crown-5-ether with 20-identical fluorine atoms surrounded by zonyl fluorosurfactant. The lipid layers were conjugated with near infrared DiR fluorescent dye for microscopic imaging experiments. Zeta potential and polydispersity index indicate the stability and heterogeneity of ZPFCE-NPs. **b** ^{19}F MR images of agar phantoms containing cells that were labeled for 24 h with 20 mM ZPFCE-NPs (fluorine concentration) were overlaid on the ^1H MR images. ^{19}F MR images are indicated as hot spots using pseudo color. Labeled BMDCs were centrifuged and counted prior to fixation in agar. (**1** = 1×10^6 , **2** = 2.5×10^6 , **3** = 5×10^6 , **w** = water). Pixels with the highest signal intensity were set to an arbitrary value of 100. **c** Quantification of the fluorine content was performed by delineation of 'hot spots' marked as the regions of interest based on the ^{19}F MR images ($R=0.9047$)

labeling was not different in the studied concentration range. The uptake of ZPFCE-NPs was quantified in the CD11c^+ MHC-II^+ BMDC rich population using flow cytometry. The percentage of BMDCs associated with ZPFCE-NPs was found to be significantly higher when ZPFCE-NPs were added during maturation compared to adding the ZPFCE-NPs

after maturation (Fig. 4a). Moreover, the amount of ZPFCE-NPs taken up during the maturation process of BMDCs was also higher as indicated by the significant increase in the mean fluorescence intensity (MFI) (Fig. 4b). This observation confirms that DCs, and in particular immature DCs, are specialized in antigen capture [15, 48]. Both percentages and

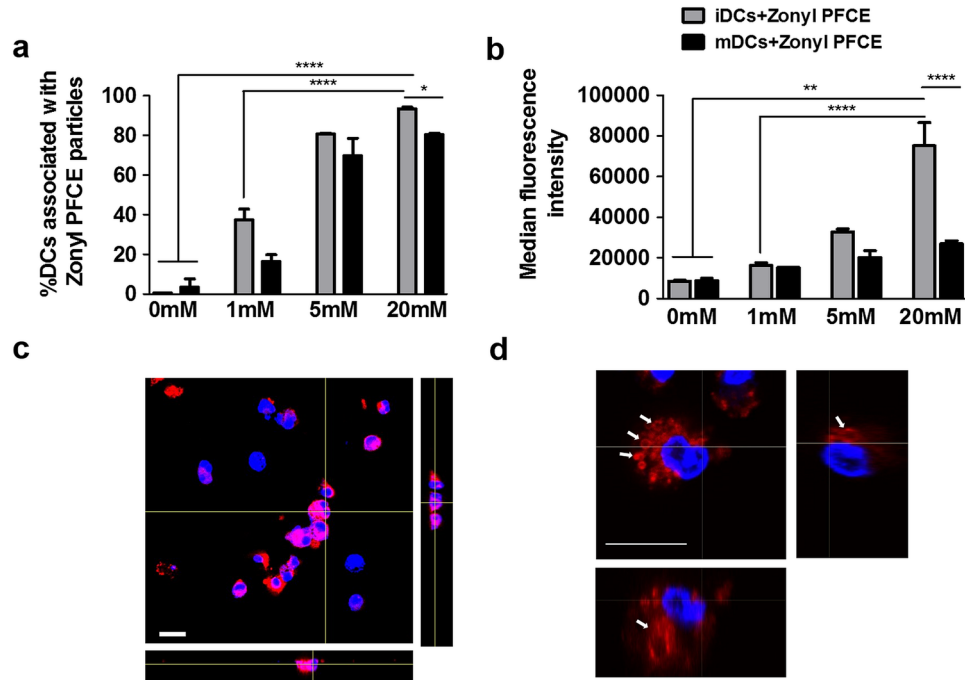


Fig. 4 In vitro analysis of ZPFCE-NPs labeled BMDCs. BMDCs were matured for 24 h in the presence of 1 mM, 5 mM or 20 mM ZPFCE-NPs (iDCs) or matured for 24 h after which 1 mM, 5 mM or 20 mM ZPFCE-NPs were added for an additional 24 h (mDCs). **a** Percentage of ZPFCE-NP⁺ cells and **b** mean fluorescence intensity (MFI) of ZPFCE-NPs in the CD11c⁺ MHC-II⁺ BMDC population was determined by flow cytometry ($n=3$). **c–d** Representative confocal microscopy images are shown as z-stacks in three dimensions of fixed iDCs confirming internalization of nanoparticles by iDCs. Nuclei were stained with Hoechst dye (blue); ZPFCE-NPs (red) are indicated with white arrows. The scale bar is 20 μm . Data are represented as mean \pm SEM. ($n=3$, * $p < 0.05$, ** $p < 0.01$, **** $p < 0.0001$)

MFI shows most efficient labeling of BMDCs with 20 mM ZPFCE-NPs (Fig. 4a–b).

Confocal microscopy illustrated the internalization of the ZPFCE-NPs in the three-dimensional scanning microscopy images of the cells. This confirmed the efficient intracellular uptake of nanoparticles by BMDCs at a concentration of 20 mM (Fig. 4c–d).

^{19}F MR Imaging of the Pancreatic Region After Adoptive Transfer of ZPFCE-NPs Labeled BMDCs

NOD/ShiLtSz-Prkdc^{scid} mice are insulinitis-free and do not develop T1D spontaneously. In our experimental setup, we used NOD.SCID mice to track the in vivo migration of BDC2.5 mimotope-loaded ZPFCE-NPs-labeled BMDCs. To induce beta cell injury, one group of mice was pre-treated with a single injection of 50 mg/kg STZ. Prior to the adoptive transfer, BMDCs were analyzed using flow cytometry to ensure viability and sufficient uptake of ZPFCE-NPs. In these experiments, ~98% of the BMDCs are ZPFCE-NPs positive (Suppl. Fig. S2a) with significantly higher particle-cell association compared to the controls (Suppl. Fig. S2b). Based on these results, 2.5×10^6 BDC2.5 mimotope-loaded ZPFCE-NPs labeled BMDCs were engrafted in the vehicle- (control group with no pancreatic inflammation) and STZ-treated groups.

Additional control NOD.SCID mice received i.p. injection of saline. Injection of STZ resulted in hyperglycemia when compared to saline injected animals 72 h after injection (Suppl. Fig. S3).

^{19}F MR imaging of all mice groups was performed. MR images of the pancreas, pancreatic lymph nodes and liver were quantified for their fluorine content. Based on the anatomical ^1H MR images, regions of interest that corresponded to the respective organs were transferred to the ^{19}F MR images, and the fluorine content was quantified relative to an external ^{19}F reference. The temporal profile of the homing of ZPFCE-NPs labeled activated BMDCs was compared between the vehicle and the STZ-treated group. A significantly higher accumulation of labeled cells was detected in the pancreas of the STZ-treated between 24 and 48 h post transfer compared to only a marginal increase in the vehicle-treated group over the same period (Fig. 5a,d). The accumulation of labeled cells was higher but not significant in the STZ-treated group at 48 h when compared to the vehicle-treated group. Interestingly, higher fluorine signal intensities (not significant) were observed and quantified in the pLNs of the vehicle-treated group as compared to the STZ-treated group (Fig. 5b). Finally, low ^{19}F MRI signal intensity from the liver of both vehicle and STZ-treated groups was acquired, indicating the deposition of a small number ZPFCE-NP-labeled BMDCs in this organ (Fig. 5c).

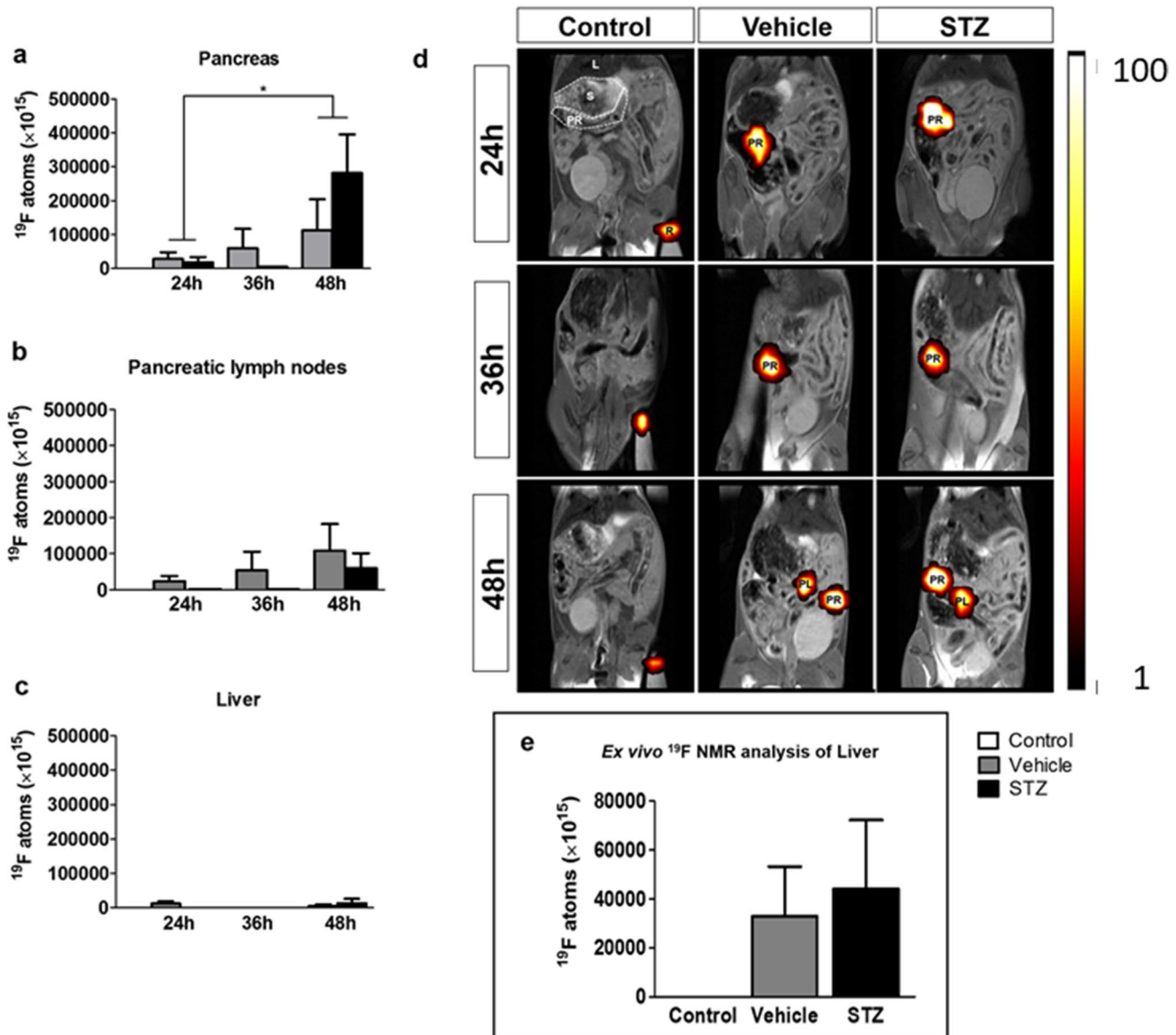


Fig. 5 Quantification and distribution of ZPFCE-NP-labeled BMDCs. At 24 h, 36 h and 48 h after adoptive transfer of BDC2.5 mimotope-loaded and ZPFCE-NP labeled BMDCs, ^{19}F MRI was performed to assess the cell distribution in vivo. **a–c** Fluorine signal was quantified as the number of fluorine atoms/pixel in the organs with high ZPFCE-NP accumulation (pancreatic region and liver) based on the overlay of ^{19}F and anatomical ^1H MR images relative to an external reference of known concentration (R). **d** In vivo ^{19}F MR images of the abdominal region of control animals (no BMDCs), vehicle- (control group with no pancreatic inflammation) and STZ-treated NOD.SCID mice ($n = 13$) showing fluorine signal due to accumulation of the ZPFCE-NP-labeled BMDCs 24 h (top), 36 h (middle) and 48 h (bottom) after cell engraftment. Pixels with the highest signal intensity were set to an arbitrary value of 100. **e** Ex vivo ^{19}F NMR based on the quantification of fluorine concentration in the liver (control animals ($n = 3$), vehicle- and STZ-treated NOD.SCID mice ($n = 5$ each)). Data represented as mean \pm SEM, $*p < 0.05$. $R = ^{19}\text{F}$ 20 mM reference, S stomach, PR pancreatic region, L liver, PL pancreatic lymph nodes. Not, threshold in the ^{19}F MR images in panel (d) are higher than those chosen for quantification of ^{19}F MRI

Additionally, ex vivo ^{19}F NMR spectroscopy was performed on liver homogenates, isolated 48 h after cell engraftment to cross-validate the quantification of in vivo ^{19}F MRI data. Indeed, the ^{19}F NMR data confirmed the in vivo ^{19}F MRI. No significant differences in the migration of ZPFCE-NPs labeled BMDCs in vehicle- and STZ-treated mice were observed (Fig. 5e).

Validation of In Vivo ^{19}F MRI by Flow Cytometry After Adoptive Transfer in NOD.SCID Mice

For further confirmation of the in vivo monitoring of BDC2.5 mimotope-loaded and ZPFCE-NP labeled BMDCs migration towards the pancreas and pLNs, a small additional cohort of vehicle ($n = 4$) and STZ-treated ($n = 4$)

NOD-SCID mice was euthanized 24 h and 48 h after adoptive transfer. Migration of labeled BMDCs towards the pancreas and pLNs was assessed by flow cytometry (Fig. 6). More ZPFCE-NP labeled BMDCs were present after 48 h compared to 24 h. However, no differences in the accumulation of ZPFCE-NP labeled BMDCs were observed between the pancreases of the vehicle- and STZ-treated mice groups. A strong reduction in ZPFCE-NPs labeled BMDCs was seen in the pLNs of STZ-treated animals but not for the vehicle-treated animals after 48 h when compared to the animals euthanized after 24 h after 48 h, suggesting that most of the ZPFCE-NP-labeled BMDCs might have migrated to the pancreas (Fig. 6g).

Discussion

Monitoring inflammation, which is implicated as a hallmark in the pathogenesis of various diseases, is gaining high interest for a better understanding of diseases and their treatment [18, 49–51]. Here, we studied DC migration with and without STZ-induced pancreatic injury, resulting in mild pancreatic inflammation. We aimed to track and quantify the migration of adoptively transferred ZPFCE-NP-labeled BMDCs towards the pancreas. The DCs have been loaded with a BDC2.5 mimotope as pancreatic antigen and as such would be expected to home to that location. Although, DC migration has already been studied by invasive techniques [45], a non-invasive follow-up of individual animals over time could provide a better insight in the sequence of events, in particular the interaction between DCs and the host.

Due to their crucial role in the balance between immunity and tolerance, DCs gained high interest during the past decade to be used in immunotherapy [52, 53]. Successful preclinical studies that have investigated the use of MRI and superparamagnetic nanoparticles to track DCs have provided promising results also for future applications of this technique in humans [54, 55]. Other studies investigated the labeling of DCs with multifunctional nanoparticles which can be incorporated with therapeutic agents, such as anticancer drugs for theranostic applications also using ^{19}F MRI for monitoring [21, 44].

Imaging techniques like ^{19}F MRI are very promising tools for the non-invasive and longitudinal study and tracking of labeled cells [31, 39, 41, 56, 57]. A major advantage of ^{19}F MRI-based cell labeling strategies is the lack of background signal and the ease to combine it with anatomical information retrieved from ^1H MRI. One disadvantage of ^{19}F MRI is its poor sensitivity [58]. To further improve the sensitivity of ^{19}F MRI, a combined approach needs to be taken, improving (a) fluorine containing contrast agents that contain high concentrations of chemically equivalent fluorine atoms [59, 60], (b) improved radio-frequency coils would further improve sensitivity [61], (c) use pulse sequences that could boost sensitivity [62] and (d) improved data processing approaches (for example, compressed sensing) [63].

PFCEs are the preferred choice for ^{19}F MRI-based cell tracking, since their 20 identical fluorine atoms partially help to overcome the methods sensitivity problems [59, 60]. Here, we report on modified PFCE-based particles for the labeling of BMDCs that are smaller and more stable than similar particles. This has resulted in a relatively high uptake of the ZPFCE-NPs by BMDCs when added during the maturation process, which is required for the in vivo tracking of labeled

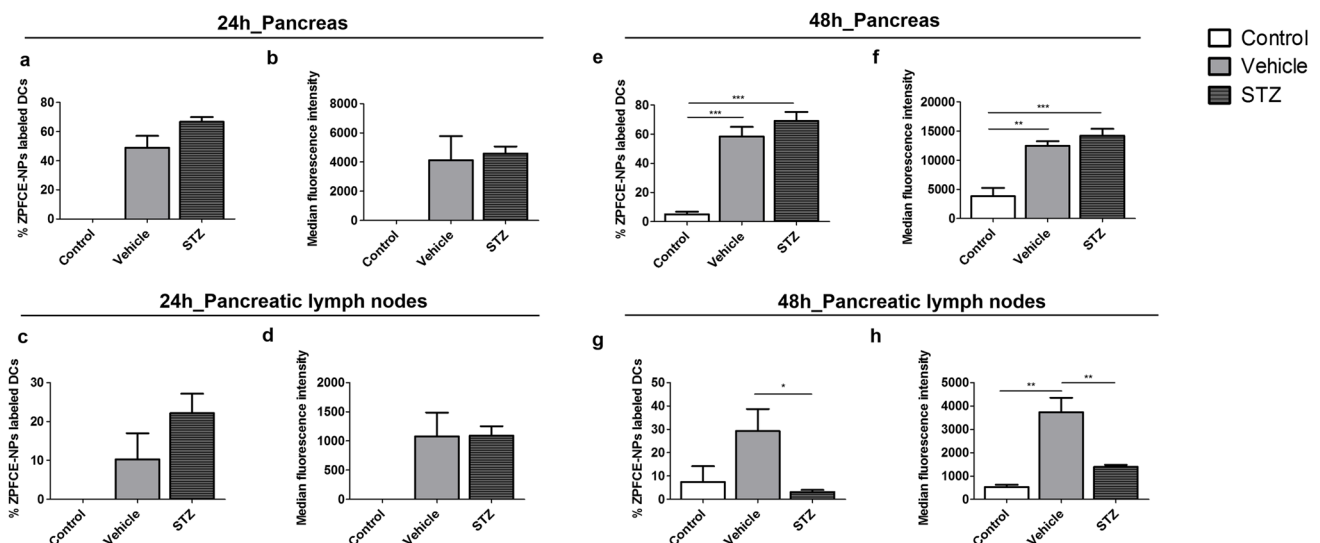


Fig. 6 Quantification of ZPFCE-NPs-labeled BMDCs isolated from control, vehicle and STZ-treated NOD.SCID mice 24 h (a–d) and 48 h (e–h) after intraperitoneal engraftment by flow cytometry. The percentage of ZPFCE-NPs⁺ cells in the CD11c⁺ MHC-II⁺ DC population was determined in the pancreas (a, e) and pLN (c, g). MFI of ZPFCE-NPs in the CD11c⁺ MHC-II⁺ DC population determined in the pancreas (b, f) and pLN (d, h). Bar graphs represent mean \pm SEM ($n=8$). * $p < 0.05$, ** $p < 0.01$, *** $p < 0.001$

cells by ¹⁹F MRI [58]. PFCEs are biologically inert compounds. Their encapsulation with various lipids is well studied with very low biological toxicity during or after the labeling procedures [37, 64–66]. It has previously been shown that different sizes of PFCE-NPs used for cell labeling result in immunogenic DCs [67]. In the current study, no adverse effects of ZPFCE-NPs labeling were detected on BMDC on viability, phenotype and function when using a concentration of 20 mM ZPFCE-NPs as cells were able to retain their functional properties.

In T1D, DCs are key players in both the prevention and induction of this autoimmune disorder. They have been extensively studied preclinically in NOD mice [14, 15, 68]. Together with self-reactive T cells, DCs remain responsible for all stages of T1D [69]. In this regard, we exploited ZPFCE-NP-labeling in order to visualize the migratory patterns of BMDC under mild inflammation. It should be noted that while pancreatic beta cell stress and destruction after low-dose STZ administration were confirmed by increased blood glucose levels 3 days after injection, the pro-inflammatory state in these STZ-induced hyperglycemic mice was not confirmed and thus was based on previous experiments [11]. Using ¹⁹F MR imaging, we showed here that BDC2.5 mimotope-loaded ZPFCE-NP-labeled BMDCs migrated with high affinity towards the pancreas after chemically induced inflammation (low dose STZ). The increased homing of BDC2.5 mimotope-loaded ZPFCE-NP-labeled BMDCs towards the inflamed pancreas could be the result of the disruption of pancreatic vasculature due to STZ-induced inflammation at 48 h. Interestingly, we identified high accumulation of fluorine atoms in the pLN of the vehicle group. This observation indicates that even without inflammatory signals BDC2.5 mimotope-loaded ZPFCE-NP-labeled BMDCs align their orientation to the pancreatic region. Based on ex vivo flow cytometry analysis of the pancreas, no significant differences were found in the number of ZPFCE-NP-labeled BMDCs of both injected groups at 24 h and 48 h. However, elevated homing of ZPFCE-NP-labeled BMDCs was noticed in the pLNs of the vehicle group in contrast to the STZ-treated group. The fact that ¹⁹F MRI reached significance and flow cytometry did not could be due to the fact that both methods measure different properties. While ¹⁹F MRI determines the fluorine content, flow cytometry measures the relative amount of labeled DCs. Apart from the pancreatic region, low ¹⁹F signal was also detectable in the liver as previously shown [45].

Briefly, in the current manuscript we established a labeling protocol for BMDCs using newly synthesized ZPFCE-NPs. Moreover, we provided a ¹⁹F MRI platform for the non-invasive imaging and quantification of BDC2.5 mimotope-loaded ZPFCE-NP-labeled BMDCs in a T1D mouse model under mild pancreatic inflammation. Future studies are required for the evaluation of the labeling and ¹⁹F MR imaging of human DCs. This could be of interest for longitudinal follow-up of tolerogenic DCs in the context of immunotherapy in T1D patients [70]. In addition, this imaging approach could also be

implemented in the development of theranostic applications using fluorinated NPs for DC vaccines in cancer, which has already been studied in humans [41, 71].

Conclusion

We demonstrated successful labeling of BMDCs with biologically compatible ZPFCE-NPs for in vivo and longitudinal follow-up of mild pancreatic inflammation in a T1D mouse model using ¹⁹F MRI. Our findings depict the feasibility of using ¹⁹F MRI and ZPFCE-NPs for monitoring and quantifying the dynamics of inflammation in T1D. Our work can potentially contribute in the further assessment of novel cell-based immunotherapies such as tolerogenic DC vaccines in the onset and progression of not only autoimmune diseases but also for novel cancer treatments.

Supplementary Information The online version contains supplementary material available at <https://doi.org/10.1007/s11307-021-01701-1>.

Acknowledgements The authors acknowledge Jos Laureys and Dries Swinnen (Clinical and Experimental Endocrinology, KU Leuven, Belgium) and Dr. Willy Gsell (Biomedical MRI, KU Leuven) for their technical assistance. We would like to thank the staff of the VIB-KU Leuven FACS Core Facility for the assistance with flow cytometry.

Funding We are grateful for the financial support by the following funding agencies: the European Commission Marie Curie (ITN) BetaTrain (289932) and INSPiRE-Med (813120), the Research Foundation Flanders (FWO, G.0A75.14, G.0B28.14, 11Y5915N and G.069115 N), the Agentschap voor Innovatie door Wetenschap en Technologie for the SBO Nano-CoMIT (IWT SBO 140061).

Declarations

Conflict of Interest Shweta Saini is currently working for Springer Nature. Other authors declare that they have no conflicts of interest.

References

1. Saberzadeh-Ardestani B, Karamzadeh R, Basiri M, Hajizadeh-Saffar E, Farhadi A, Shapiro AMJ, Tahamtani Y, Baharvand H (2018) Type 1 diabetes mellitus: cellular and molecular pathophysiology at a glance. *Cell J* 20:294–301
2. Pietropaolo M Pathogenesis of type 1 diabetes mellitus. <http://www.Uptodate.com/Contents/Pathogenesis-of-Type-1-Diabetes-Mellitus>. Accessed 28 Mar 2021
3. Wucherpfennig KW, Eisenbarth GS (2001) Type 1 diabetes. *Nature* 2:767–768
4. Maahs DM, West NA, Lawrence JM, Mayer-Davis EJ (2010) Epidemiology of type 1 diabetes. *Endocrinol Metab Clin N Am* 39:481
5. Rewers M, Ludvigsson J (2016) Environmental risk factors for type 1 diabetes. *Lancet* 387:2340–2348
6. Morran MP, Vonberg A, Khadra A, Pietropaolo M (2015) Immunogenetics of type 1 diabetes mellitus. *Mol Aspects Med* 42:42–60
7. Eizirik DL, Colli ML, Ortis F (2009) The role of inflammation in insulinitis and beta-cell loss in type 1 diabetes. *Nat Rev Endocrinol* 5:219–226
8. Cabrera SM, Henschel AM, Hessner MJ (2016) Innate inflammation in type 1 diabetes. *Transl Res* 167:214–227
9. Furman BL (2015) Streptozotocin-induced diabetic models in mice and rats. *Curr Protoc Pharmacol* 70:5.47.1–5.47.20
10. Wu J, Yan LJ (2015) Streptozotocin-induced type 1 diabetes in rodents as a model for studying mitochondrial mechanisms of diabetic β cell glucotoxicity. *Diabetes Metab Syndr Obes Targets Ther* 8:181–188

11. Niu S, Bian Z, Tremblay A, Luo Y, Kidder K, Mansour A, Zen K, Liu Y (2017) Broad infiltration of macrophages leads to a proinflammatory state in streptozotocin-induced hyperglycemic mice. *J Immunol* 197:3293–3301
12. Martin AP, Alexander-Brett JM, Canasto-Chibuque C, Garin A, Bromberg JS, Fremont DH, Lira SA (2007) The chemokine binding protein M3 prevents diabetes induced by multiple low doses of streptozotocin. *J Immunol* 178:4623–4631
13. Luo Z, Soläng C, Mejia-Cordova M, Thorvaldson L, Blixt M, Sandler S, Singh K (2019) Kinetics of immune cell responses in the multiple low-dose streptozotocin mouse model of type 1 diabetes. *FASEB Bioadv* 1:538–549
14. Morel PA (2013) Dendritic cell subsets in type 1 diabetes: friend or foe? *Front Immunol* 4:415
15. Mellman I, Steinman RM (2001) Dendritic cells: specialized and regulated antigen processing machines. *Cell* 106:255–258
16. Kaliński P, Hilkens CMU, Wierenga EA, Kapsenberg ML (1999) T-cell priming by type-1 and type-2 polarized dendritic cells: the concept of a third signal. *Immunol Today* 20:561–567
17. Pletinckx K, Döhler A, Pavlovic V, Lutz MB (2011) Role of dendritic cell maturity/costimulation for generation, homeostasis, and suppressive activity of regulatory T cells. *Front Immunol* 2:39
18. Lehuen A, Diana J, Zaccone P, Cooke A (2010) Immune cell crosstalk in type 1 diabetes. *Nat Rev Immunol* 10:501–513
19. Gillespie KM (2006) Type 1 diabetes: pathogenesis and prevention. *Can Med Assoc J* 175:165–170
20. Yoon JW, Jun HS (2005) Autoimmune destruction of pancreatic β cells. *Am J Ther* 12:580–591
21. Ahrens ET, Flores R, Xu H, Morel PA (2005) In vivo imaging platform for tracking immunotherapeutic cells. *Nat Biotechnol* 23:983–987
22. Perrin J, Capitaio M, Mouglin-Degraef M, Guerard F, Faivre-Chauvet A, Rbah-Vidal L, Gaschet J, Guilloux Y, Kraeber-Bodere F, Cherel M, Barbet J (2020) Cell tracking in cancer immunotherapy. *Front Med* 7:e34
23. Chapelin F, Capitini CM, Ahrens ET (2018) Fluorine-19 MRI for detection and quantification of immune cell therapy for cancer. *J Immunother Cancer* 6:e105
24. Pan W, Zheng X, Chen GY, Su LH, Luo SH, Wang W, Ye SD, Weng JP, Min Z (2020) Nanotechnology's application in Type 1 diabetes. *Wiley Interdiscip Rev Nanomed Nanobiotechnol* 12:e1645
25. Gaglia JL, Guimaraes AR, Harisinghani M, Turvey SE, Jackson R, Benoist C, Mathis D, Weissleder R (2011) Noninvasive imaging of pancreatic islet inflammation in type 1A diabetes patients. *J Clin Invest* 121:442–445
26. O'Neill E, Hammond N, Miller FH (2014) MR imaging of the pancreas. *Radiol Clin North Am* 52:757
27. Wu C, Li F, Niu G, Chen X (2013) PET imaging of inflammation biomarkers. *Theranostics* 3:448–466
28. Gaglia JL, Harisinghani M, Aganj I, Wojtkiewicz GR, Hedgire S, Benoist C, Mathis D, Weissleder R (2015) Noninvasive mapping of pancreatic inflammation in recent-onset type-1 diabetes patients. *Proc Natl Acad Sci* 112:2139–2144
29. Thoeni RF (2015) Imaging of acute pancreatitis. *Radiol Clin North Am* 53:1189
30. Mallak N, Hope TA, Guimaraes AR (2018) PET/MR imaging of the pancreas. *Magn Reson Imaging Clin N Am* 26:345
31. Liang S, Louchami K, Holvoet B, Verbeke R, Deroose CM, Manshian B, Soenen SJ, Lentacker I, Himmelreich U (2018) Tri-modal in vivo imaging of pancreatic islets transplanted subcutaneously in mice. *Mol Imaging Biol* 20:940–951
32. Vandeputte C, Thomas D, Dresselaers T, Crabbe A, Verfaillie C, Baekelandt V, Van Laere K, Himmelreich U (2011) Characterization of the inflammatory response in a photothrombotic stroke model by MRI: implications for stem cell transplantation. *Mol Imaging Biol* 13:663–671
33. Weber R, Wegener S, Ramos-Cabrera P, Wiedermann D, Hoehn M (2005) MRI detection of macrophage activity after experimental stroke in rats: new indicators for late appearance of vascular degradation? *Magn Reson Med* 54:59–66
34. Temme S, Bönner F, Schrader J, Flögel U (2012) 19F magnetic resonance imaging of endogenous macrophages in inflammation. *Wiley Interdiscip Rev Nanomed Nanobiotechnol* 4:329–343
35. Weise G, Basse-Luesebrenk TC, Wessig C, Jakob PM, Stoll G (2011) In vivo imaging of inflammation in the peripheral nervous system by 19F MRI. *Exp Neurol* 229:494–501
36. Ebner B, Behm P, Jacoby C, Burghoff S, French BA, Schrader J, Flögel U (2010) Early assessment of pulmonary inflammation by 19F MRI in vivo. *Circ Cardiovasc Imaging* 3:202–210
37. Srinivas M, Heerschap A, Ahrens ET, Figdor CG, de Vries IJM (2010) 19F MRI for quantitative in vivo cell tracking. *Trends Biotechnol* 28:363–370
38. Stoll G, Basse-Lüsebrink T, Weise G, Jakob P (2012) Visualization of inflammation using 19F-magnetic resonance imaging and perfluorocarbons. *Wiley Interdiscip Rev Nanomed Nanobiotechnol* 4:438–447
39. Tirotta I, Dichiarante V, Pigliacelli C, Cavallo G, Terraneo G, Bombelli FB, Metrangolo P, Resnati G (2015) 19F magnetic resonance imaging (MRI): from design of materials to clinical applications. *Chem Rev* 115:1106–1129
40. Balducci A, Helfer BM, Ahrens ET, O'Hanlon CF, Wesa AK (2012) Visualizing arthritic inflammation and therapeutic response by fluorine-19 magnetic resonance imaging (19F MRI). *J Inflamm* 9:24
41. Ahrens ET, Helfer BM, O'Hanlon CF, Schirda C (2014) Clinical cell therapy imaging using a perfluorocarbon tracer and fluorine-19 MRI. *Magn Reson Med* 72:1696–1701
42. Srinivas M, Tel J, Schreiber G, Bonetto F, Cruz L-J, Amiri H, Heerschap A, Figdor CG, de Vries IJM (2015) PLGA-encapsulated perfluorocarbon nanoparticles for simultaneous visualization of distinct cell populations by ¹⁹F MRI. *Nanomedicine* 10:2339–2348
43. Saini S, Poelmans J, Korf H, Dooley JL, Liang S, Manshian BB, Verbeke R, Soenen SJ, Vande Velde G, Lentacker I, Lagrou K, Liston A, Gysemans C, De Smedt SC, Himmelreich U (2019) Longitudinal in vivo assessment of host-microbe interactions in a murine model of pulmonary aspergillosis. *iScience* 20:184–194
44. Dewitte H, Geers B, Liang S, Himmelreich U, Demeester J, De Smedt SC, Lentacker I (2013) Design and evaluation of theranostic perfluorocarbon particles for simultaneous antigen-loading and 19F-MRI tracking of dendritic cells. *J Control Release* 169:141–149
45. Ferreira GB, Gysemans CA, Demengeot J, da Cunha JPMCM, Vanherwegen A-S, Overbergh L, Van Belle TL, Pauwels F, Verstuyf A, Korf H, Mathieu C (2014) 1,25-Dihydroxyvitamin D3 promotes tolerogenic dendritic cells with functional migratory properties in NOD mice. *J Immunol* 192:4210–4220
46. Trekker J, Leten C, Struys T, Lazenka VV, Argibay B, Micholt L, Lambrechts I, Van Roy W, Lagae L, Himmelreich U (2014) Sensitive in vivo cell detection using size-optimized superparamagnetic nanoparticles. *Biomaterials* 35:1627–1635
47. Staelens D, Liang S, Appeltans B, Van de Wouwer M, Van den Mooter G, Van Assche G, Himmelreich U, Vande VG (2016) Visualization of delayed release of compounds from pH-sensitive capsules in vitro and in vivo in a hamster model. *Contrast Media Mol Imaging* 11:24–31
48. Steinman RM (1991) The dendritic cell system and its role in immunogenicity. *Annu Rev Immunol* 9:271–296
49. Eizirik DL, Colli ML, Ortis F (2009) The role of inflammation in insulinitis and β -cell loss in type 1 diabetes. *Nat Rev Endocrinol* 5:219–226
50. Lyman M, Lloyd DG, Ji X, Vizcaychipi MP, Ma D (2014) Neuroinflammation: the role and consequences. *Neurosci Res* 79:1–12
51. Willerson JT, Ridker PM (2004) Inflammation as a cardiovascular risk factor. *Circulation* 109:2–10
52. Boudewijns S, Bloemendal M, Gerritsen WR, de Vries IJM, Schreiber G (2016) Dendritic cell vaccination in melanoma patients: from promising results to future perspectives. *Hum Vaccines Immunother* 12:2523–2528
53. Hori Y, Winans AM, Huang CC, Horrigan EM, Irvine DJ (2008) Injectable dendritic cell-carrying alginate gels for immunization and immunotherapy. *Biomaterials* 29:3671–3682
54. Baumjohann D, Hess A, Budinsky L, Brune K, Schuler G, Lutz MB (2006) In vivo magnetic resonance imaging of dendritic cell migration into the draining lymph nodes of mice. *Eur J Immunol* 36:2544–2555
55. De Vries IJM, Lesterhuis WJ, Barents JO, Verdijk P, Van Krieken JH, Boerman OC, Oyen WJG, Bonenkamp JJ, Boezeman JB, Adema GJ, Bulte JWM, Scheenen TWJ, Punt CJA, Heerschap A, Figdor CG (2005) Magnetic resonance tracking of dendritic cells in melanoma patients for monitoring of cellular therapy. *Nat Biotechnol* 23:1407–1413
56. Chen J, Lanza GM, Wickline SA (2010) Quantitative magnetic resonance fluorine imaging: today and tomorrow. *Wiley Interdiscip Rev Nanomed Nanobiotechnol* 4:431–440

57. Hitchens TK, Ye Q, Eytan DF, Janjic JM, Ahrens ET, Ho C (2011) 19F MRI detection of acute allograft rejection with in vivo perfluorocarbon labeling of immune cells. *Magn Reson Med* 4:1145–1154
58. Saini S, Korf H, Liang S, Verbeke R, Manshian B, Raemdonck K, Lentacker I, Gysemans C, De Smedt SC, Himmelreich U (2019) Challenges for labeling and longitudinal tracking of adoptively transferred autoreactive T lymphocytes in an experimental type-1 diabetes model. *Magn Reson Mater Physics Biol Med* 32:295–305
59. Kok MB, De Vries A, Abdurrachim D, Prompers JJ, Grüll H, Nicolay K, Strijkers GJ (2011) Quantitative 1H MRI, 19F MRI, and 19F MRS of cell-internalized perfluorocarbon paramagnetic nanoparticles. *Contrast Media Mol Imaging* 6:19–27
60. Jacoby C, Temme S, Mayenfels F, Benoit N, Krafft MP, Schubert R, Schrader J, Flögel U (2014) Probing different perfluorocarbons for in vivo inflammation imaging by 19F MRI: image reconstruction, biological half-lives and sensitivity. *NMR Biomed* 27:261–271
61. Waiczies S, Millward JM, Starke L, Delgado PR, Huelnhagen T, Prinz C, Marek D, Wecker D, Wissmann R, Koch SP, Boehm-Sturm P, Waiczies H, Niendorf T, Pohlmann A (2017) Enhanced fluorine-19 MRI sensitivity using a cryogenic radiofrequency probe: technical developments and ex vivo demonstration in a mouse model of neuroinflammation. *Sci Rep* 7:9808
62. Meissner M, Reiser M, Hugger T, Hennig J, von Elverfeldt D, Leupold J (2015) Revealing signal from noisy F-19 MR images by chemical shift artifact correction. *Magn Reson Med* 73:2225–2233
63. Liang S, Dresselaers T, Louchami K, Zhu C, Liu Y, Himmelreich U (2017) Comparison of different compressed sensing algorithms for low SNR F-19 MRI applications—imaging of transplanted pancreatic islets and cells labeled with perfluorocarbons. *NMR Biomed* 30:3776
64. Srinivas M, Boehm-Sturm P, Figdor CG, de Vries JJ, Hoehn M (2012) Labeling cells for in vivo tracking using 19F MRI. *Biomaterials* 33:8830–8840
65. Chung BH, Lim YT (2009) Cell labeling and imaging using multifunctional perfluorocarbon nanoemulsion. Patent Cooperation Treaty Int Appl WO/2009/128610
66. Oliva J, Bardag-Gorce F, Wood A, Sota H, Niihara Y (2015) Direct labeling of 19F-perfluorocarbon onto multilayered cell sheet for MRI-based non-invasive cell tracking. *Tissue Eng Regen Med* 12:371–378
67. Waiczies H, Lepore S, Janitzek N, Hagen U, Seifert F, Ittermann B, Purfürst B, Pezzutto A, Paul F, Niendorf T, Waiczies S (2011) Perfluorocarbon particle size influences magnetic resonance signal and immunological properties of dendritic cells. *PLoS One* 6:21981
68. Serreze DV, Gaskins HR, Leiter EH (1993) Defects in the differentiation and function of antigen presenting cells in NOD/Lt mice. *J Immunol* 150:2534–2543
69. Calderon B, Unanue ER (2012) Antigen presentation events in autoimmune diabetes. *Curr Opin Immunol* 24:119–128
70. Maldonado RA, von Andrian UH (2010) How tolerogenic dendritic cells induce regulatory T cells. *Adv Immunol* 108:111–165
71. Fink C, Gaudet JM, Fox MS, Bhatt S, Viswanathan S, Smith M, Chin J, Foster PJ, Dekaban GA (2018) 19F-perfluorocarbon-labeled human peripheral blood mononuclear cells can be detected in vivo using clinical MRI parameters in a therapeutic cell setting. *Sci Rep* 8:590

Publisher's Note Springer Nature remains neutral with regard to jurisdictional claims in published maps and institutional affiliations.